NSLS-II BPM AND FAST ORBIT FEEDBACK SYSTEM*

Om Singh[#], Belkacem Bacha, Alexei Blednykh, Weixing Cheng, L. R. Dalesio, Christopher Danneil, Joseph De Long, Al Joseph Della Penna Jr., Kiman Ha, Yong Hu, Bernard Nicolas Kosciuk, Marshall Albert Maggipinto, Joe Mead, Danny Padrazo, Igor Pinayev, Yuke Tian, Kurt Vetter, Li-Hua Yu, NSLS-II, Brookhaven National Laboratory, Upton, NY 11973

Abstract

The National Synchrotron Light Source II (NSLS-II) is a third generation light source under construction at Brookhaven National Laboratory. The project includes a highly optimized, ultra-low emittance, 3GeV electron storage ring, linac pre-injector and full energy booster synchrotron. The low emittance requires high-performance beam position monitor systems (BPMS), providing measurement to better than 200nm resolution; and fast orbit feedback (FOFB) systems, holding orbit to similar levels of orbit deviations. The NSLS-II storage ring has 30 cells, each deploying up to 9 RF BPMSs and 3 fast weak correctors. Each cell consists of a "cell controller," providing fast orbit feedback system infrastructure. This paper will provide a description of system design and summarize the implementation and status for these systems.

INTRODUCTION

NSLS-II, a 3GeV ultra-low emittance third generation light source, is in the advanced stages of construction at Brookhaven National Laboratory [1,2]. The injector consists of a 200MeV linac, transport lines, 3GeV ramping booster synchrotron, and the storage ring injection straight section [3]. The linac commissioning was conducted successfully during Spring 2012 [4], with remaining injector commissioning to start in Fall 2013. The storage ring has 30 cells (15 super-periods) with 15 low-beta (short) straights and 15 high-beta (long) straights [5]. The electron beam size at the center of the short straights has smallest rms vertical beam size of 3.1 μm (Table 1); and with 10% beam stability requirement, the orbit needs to be held below the 0.3 μm level at these locations.

Table 1: Electron Beam Size at the Various Source Locations

Types of source	Long ID	3-pole wiggler	Bend magnet	Short ID
σ_x (μm)	108	175	44.2	29.6
σ_y (μm)	4.8	12.4	15.7	3.1

To achieve such small orbit deviation, considerable effort has been devoted during the development phases to optimizing many systems relating to orbit measurement,

such as RF BPM button geometry, support structure, and RF BPM electronics. The high level of temperature stability (±0.1°C in both storage ring tunnel and electronic racks) will play an important role in achieving stable system performance for mechanical and electronics systems [6-8]. The efforts have also been devoted to develop novel approaches to NSLS-II fast-orbit feedback system, along with development of a high-speed serial data interface and cell controller [9-11].

BPM SUB-SYSTEMS STATUS

RF BPM Button Geometry Optimization

There are six RF BPMs in each cell, with a total of 180 in the storage ring (SR). In addition, there are up to three RF BPMs in each straight section where insertion device(s) (IDs) are installed. The RF BPM button geometry optimization was applied to maximize high position sensitivities and minimize thermal and trapped mode heating effects [12-15]. This resulted in a two-button assembly configuration, shown in Fig. 1, requiring two assemblies, mounted on top and bottom of the vacuum chamber.
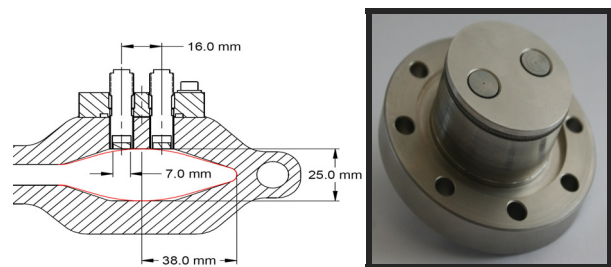

Figure 1: The large aperture (LA) RF BPM button assembly design with two buttons in a single flange (left-only top assembly shown). A production unit is shown on the right.

The LA RF button assemblies (rotated) are also used in straight sections where IVUs are installed. The RF BPM buttons were also optimized for small aperture (SA) vacuum chambers for damping wigglers (DWs) and elliptically polarized undulators (EPUs) [16]. The geometry details for all types are given in Table 2 [17].

A total of 500 LA RF button assemblies were procured from Times Microwave, Inc.; these have all been received, tested, and installed. A procurement of 65 SA RF button assemblies is in production from MPF, Inc. and

will be available in time for installation in the insertion device vacuum chambers.

Table 2: NSLS-II BPM Geometry/Sensitivities

	LA RF BPM		SA RF BPM	
	Multi-pole LA-BPM	IVU LA-64deg	DW SA-60deg	EPU SA-60deg
Chamber size (h*v) (mm)	76*25	76*25	60*11.5	60*8
Button diameter	7	7	4.7	4.7
Button gap	0.25	0.25	0.25	0.25
Button thickness	2	2	2	2
Button h-sep	16	7	5	5
S1- y [/mm]	0.084	0.114	0.226	0.294
S1 - x [/mm]	0.090	0.070	0.131	0.217

RF BPM - Rogue Mode Coupling

A rogue mode RF shielding [18] has been successfully designed and implemented into all 90 multi-pole vacuum chambers' antechamber slots, as shown in Fig. 2. The installation of this shield (BeCu springs) resulted in shifting the high order modes (HOM) from the BPM frequency region (499.68 MHz) to an out-of-band frequency region (> 800 MHz). Due to synchrotron radiation proximity in the S6 multi-pole vacuum chamber, the RF shielding strip must be shortened, making it impossible to shift HOM for the 6th BPM (last BPM in the cell). If HOM modes fall within the BPM frequency band at this location, a nearby BPM in the straight section will be used instead.
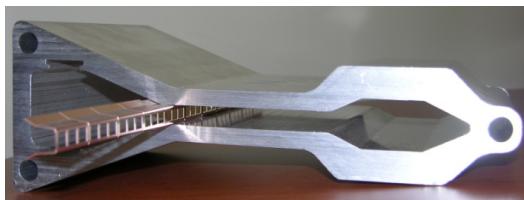

Figure 2: Flexible BeCu RF shielding with 50% of opening space inside of the multi-pole vacuum chamber. The thickness of the RF shield is 0.25 mm.

RF BPM Button Vacuum Chamber Support

The multi-pole vacuum chamber, housing RF buttons, is suspended on a set of thermally stable mechanical supports built from low thermal expansion material carbon fiber [19]. Fig. 3 (left) shows a set of carbon fiber supports, mounted on a stable magnet girder [6]. The overall thermal stability at the RF button location has been measured to be < 200 nm. The straight section supports for IVUs, shown in Fig. 3 (right) are built from Invar rod, providing < 100 nm thermal stability with SR tunnel air temperature variation of ± 0.1°C [20]. Both types of supports meet the thermal stability requirements.

The vibration stability for stands has also been studied [21]. The vibration measurement made in 2009 showed the ground floor motion to be 29 nm in the 4–100 Hz frequency band; while the motion on top of the stand was

71 nm in the horizontal plane, meeting the 100 nm requirement. However, recent measurements [21] indicate that ground floor motion on the NSLS-II site is much larger - as much as 5 times larger, if the 2-4 Hz band is considered. Further work is in progress to investigate and mitigate these high level of ground motion, but expectations are that the fast-orbit feedback should be able to maintain overall noise levels to < 200 nm.
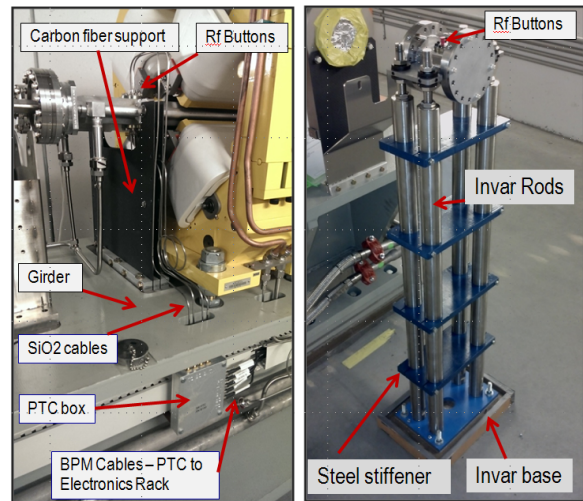

Figure 3: Thermally stable supports for multi-pole section (left) and IVUs straight section (right) vacuum chambers.

RF BPM Electronics and Controls

The RF BPM electronics development was undertaken to create a state-of-the-art BPM with a goal of exceeding capabilities and performance that has been demonstrated to date [11,22,23]. The added motivation for in-house design was also to have resident experts as the facility matures and new requirements emerge. The architecture of the RF BPM electronics has been carefully conceived to provide robust design with substantial flexibility to serve as a platform for other systems.

The RF BPM electronics system consists of 1) a chassis housing an analog front-end (AFE), digital front-end (DFE), and power supply (PS) modules, shown in Fig. 4;
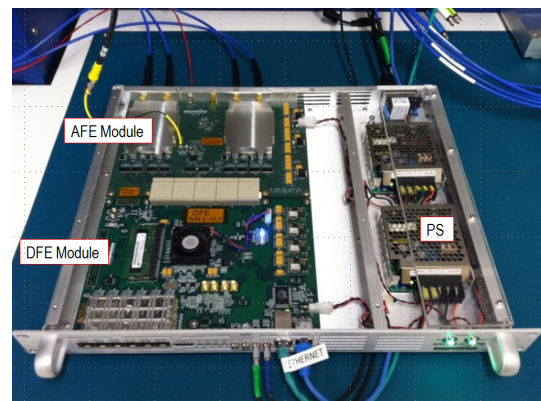

Figure 4: NSLS-II RF BPM electronics chassis with AFE, DFE, and PS modules.

and 2) a pilot tone combiner (PTC) module mounted in the tunnel near the RF buttons, shown in Fig. 3 (left).

The AFE topology is based on band-pass sampling architecture, which subsamples the 500MHz impulse response of the SAW band-pass filter at ~117 MHz. The response of the filter produced for a single bunch results in an impulse of approximately 30 samples or ~300 ns in length. Coherent timing is derived from an external 378KHz revolution clock via differential CML. An analog phase-locked loop is used to synchronize a VCXO ADC clock synthesizer. The received revolution clock is transmitted to the DFE to serve as a time reference for the digital signal processing (DSP) engine.

The DFE is responsible for all DSP of the button signals and communication of the results with the control system. The DFE is based on a Xilinx Virtex-6 Field Programmable Gate Array (FPGA). The fixed-point DSP engine calculates TbT position based on a single-bin DFT algorithm. The FOFB 10KHz data and 10Hz slow acquisition data are derived directly from the TbT calculation.

The BPM system is parametrically configured for single-pass, booster, or storage ring. The DSP architecture is also generic; all three operational modes are derived from storage ring revolution frequency.

An industrial PC running the Linux Operating System (Debian) supports waveform monitoring for ADC raw data, single pass, turn-by-turn, fast data, and slow data. The ADC raw, TbT, and FA data are triggered on demand and support a large 1-million sample history buffer. Table 3 provides a summary for all data transfer capabilities.

Table 3: RF BPM Data Transfer Capabilities

Data Type	Mode	Max Length
ADC Data (117 MHz)	On-demand	256 Mbytes or 32M samples per channel simultaneously
Single-Pass	Streaming	800hr circular buffer (1Hz Injection)
TbT (378 kHz)	On-demand	256 Mbytes or 5 M samples Va,Vb,Vc,Vd, X,Y,SUM, Q, pt_va,pt_vb,pt_vc,pt_vd
Fast Acquisition Data - FA (10KHz)	Streaming via SDI Link & On-demand	Streaming - X,Y; For on demand: 256 Mbytes or 5 Msamples. Va,Vb,Vc,Vd, X,Y, SUM, Q, pt_va,pt_vb,pt_vc,pt_vd
Slow Acquisition SA (10Hz)	Streaming and On-demand	80hr circular buffer - Va,Vb,Vc,Vd, X,Y,SUM, Q, pt_va,pt_vb,pt_vc,pt_vd
System Health (10 Hz)	Streaming & on-demand	80hr circular buffer AFE temp, DFE temp, FPGA Die temp, PLL lock status, SDI Link status
FFT Coefficients	On-demand	DC – 10 kHz, 10 Hz resolution.

The PTC, shown in Fig. 5, is a passive module located on the girder below the RF button. A 1m SiO2 cable connects the RF button to the PTC module, shown in Fig. 3 (left). A pilot tone generated on the AFE is carried out to the PTC module via a 5th cable, which is coupled into

each of four forward-beam signal channels. The pilot tone was to be used to provide dynamic calibration to mitigate long-term drift. However, tests have shown that the BPM long-term stability (< 200 nm) has been achieved by the use of highly stable ±0.1°C thermally regulated racks [23]. The pilot tone now is only used for system diagnostics and integration while no beam is present and is discussed later.
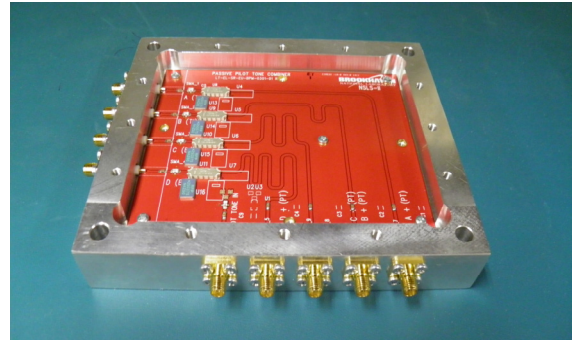

Figure 5: Pilot Tone Combiner (PTC).

Test Results and Installation Status

The NSLS-II RF BPM program began in August of 2009. Successful beam tests [22] were conducted at 1) the Advanced Light Source (ALS) 15 months into the program; and at 2) NSLS-II during the linac commissioning period in May, 2012. In a 2kHz frequency band, the measured position resolution at the ALS storage ring is less than 1 μm in single bunch (25 mA) and 0.2 μm in multi-bunch (500 mA) modes. The measured resolution at the NSLS-II linac BPM #1 is 4 μm (shown in Fig. 6), whereas the requirement is 10 μm. The RF BPM electronic performance as measured with beam exceeded the requirement.

Figure 6: NSLS-II Linac BPMS control panel. The 1st BPM, configured for noise measurement, shows the electronic noise < 4 μm.

The production and system test of 275 RF BPM electronics units have been completed. The installation and the integrated test have also been completed for the injector RF BPMs (total injector BPMs = 56). The installation of storage ring RF BPMs has been completed; integrated testing is in progress and will be completed by November, 2013. The storage ring commissioning is planned to start in March, 2014.

The pilot tone test signal, built into the BPM system, has proved to be an excellent diagnostic and system integration tool; it is being used currently in the field tests. The pilot tone is set to the BPM frequency at 499.68 MHz and must be turned on. Since, the pilot tone signal is coupled into the path of the beam signal, thereby providing beam-equivalent signals. The basic functionality of BPMs is checked by collecting raw ADC, TbT, and FA data and analyzing in the frequency spectrum and time domain. Table 4 below shows test data taken for a booster BPM in the field using pilot tone. The four data sets were collected at four different power levels by setting the pilot tone attenuator, built into the pilot tone circuit. The FA data (10 kHz) shows noise level to be nominal; 300 nm at -14.7 dBFS and 6 µm at -44.7 dBFS power level; with 0 dBFS equivalent to FS ADC count.

Table 4: Booster BPM FA Data Collected with Pilot Tone

PT atten dB	ADC pwr (dBFS)	FA-X pos	FA-X std	FA-Y pos	FA-Y std
0.0	-14.7	197.8	0.3	314.6	0.2
10.0	-24.5	192.0	0.6	308.9	0.5
20.0	-34.4	176.1	1.8	295.1	1.4
30.0	-44.7	121.8	6.0	235.9	4.7

During early testing, spurious noise signals were picked up in the AFE module, related to the signal pickup from the DFE module via the RF BPM chassis top cover. The interfering signal was emitted from several sources within DFE module, inducing a current on the BPM top cover and coupling into the receiver input. This effect varies from BPM to BPM and was predominant at low input signal levels. For example, ~500 Hz spurious signals were observed in the FA frequency spectrum for a booster BPM (A1PKU3) as shown in Fig. 7 (top).
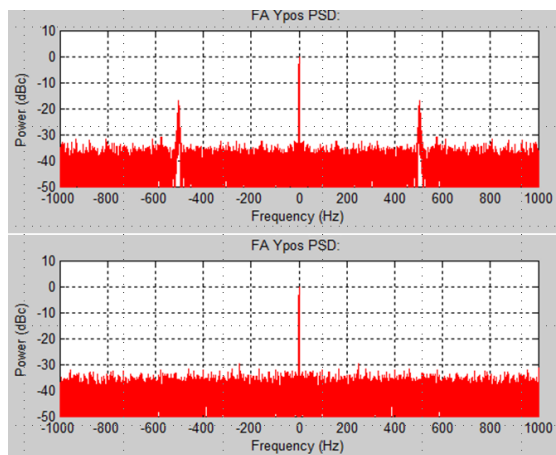

Figure 7: A 500 Hz spurious signal is observed in the FA data spectrum (top), due to noise pickup in AFE. The bottom plot shows spurious signals have been eliminated after installation of a 4"x6 " micro-wave absorber.

This was quickly resolved by installing a 4″x 6″ microwave absorber (RFLS 5092) on the inside cover of the chassis enclosure which absorbs the interfering electric field thereby eliminating the interfering current induced on the top cover – as shown in the bottom plot of Fig. 7. Note that DC peak of 1 µm (equivalent to 0 dBc power) has been inserted for noise calibration on the plot. So, the 500Hz signal noise level, shown in the top of Fig. 7 plot, is about 100 nm.

BPM Calibration and Diagnostics

To get accurate beam position measurements, the sensitivity curves have been calculated and fitted by 5th order polynomials [17] for various types of RF BPM geometries. To benefit the early stage of commissioning, the offset between the chamber geometry center and the BPM electric center are being measured, as well [24].

The BPM sum signal will be corrected for large position offsets errors on a turn-by-turn basis [24]. The cable lengths will also be factored in. This would enable monitoring of beam losses, providing a useful tool during the early days of commissioning. The BPM Q signal will provide health status of BPM functionality; it will be tracked and any abnormalities will be flagged to the operator

FAST ORBIT FEEDBACK (FOFB) STATUS

Fast Corrector DC/AC Requirement

The orbit effect due to ground vibration is expected to be 4–7 µm in the 2–10 Hz frequency band without fast-orbit correction [21], and an order lower at frequency > 10 Hz. In order to achieve the 100nm level of orbit stability, the feedback system gain at low frequency must be at least 70. A system with DC gain of 100 has been proposed, with one pole corner frequency at 3 Hz. A Bode magnitude plot of this feedback model is shown in Fig. 8 with combined (BPM & Corrector), controller, and overall responses. The overall response curve has zero cross-over at 300 Hz, and 8 dB gain margin measured when the phase cross-over is 180 degrees (phase plot not shown).
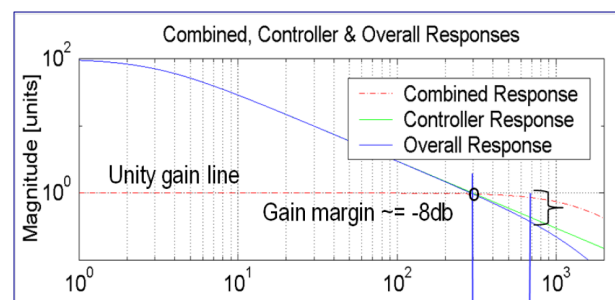

Figure 8: A magnitude Bode plot of the simple feedback model. Phase plot is not shown.

The air core corrector was chosen for the fast correctors due to its simple design, small profile (60mm length),

short fringe field, and low cost [25]. The fast-corrector power supply DC strength has been specified to be 15 µrad, with small signal bandwidth of > 5 kHz [26]. The corrector inductance results in a bend (one pole) at about 10 Hz. Fig. 9 shows the corrector system AC specification, along with correction requirements for noise suppression from various sources - DC drift, vibration, and ID gap change effects.
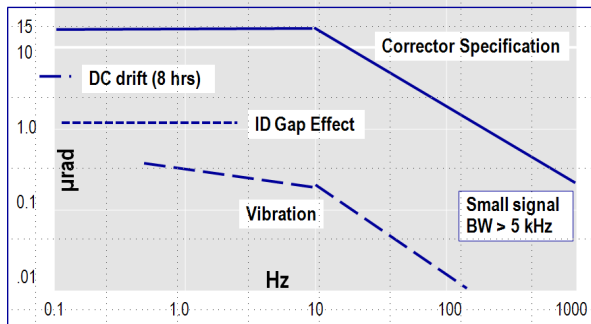

Figure 9: The corrector system AC specification and corrector requirement to suppress various noise sources

In each cell, there are three fast, weak correctors utilized for fast-orbit correction; and six slow, strong correctors utilized for slow-orbit correction and/or orbit alignment. The location of slow and fast correctors and BPMs in one cell is shown in Fig. 10. In case, the fast corrector DC strength may not be sufficient for long-term drift correction, the fast corrector DC component will be moved out to slow correctors at some interval to avoid saturation of the fast corrector power supply [9]. This technique has already been implemented into operation at Soleil [27].
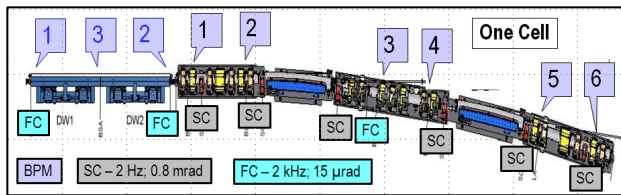

Figure 10: One cell with six slow correctors, three fast correctors, and up to nine RF BPMs.

Fast Orbit Feedback Principles

An orbit feedback system includes many BPMs to monitor the orbit and many correctors to adjust the orbit. From a control theory point of view, it is a typical multiple-input multiple-output (MIMO) system. Singular value decomposition (SVD) is commonly used for the orbit feedback calculation [9,28]. To correct the ill-conditioned response matrix, truncated SVD (TSVD) and Tikhonov regulation is also often applied to improve the orbit feedback performance.

One common feature for the traditional SVD-based orbit feedback algorithm is that it applies the same controller dynamics to all eigenmodes. For better

understanding and better control of the orbit feedback system, it is advantageous to convert the MIMO problem into many single input single output (SISO) problems in eigenspace. Such conversion allows us to measure and analyze each eignemode in the frequency domain and to design the corresponding compensation for each eignenmode. This approach provides many benefits, both for system analysis and orbit correction. The challenge for such individual eigenmode compensation is that the feedback system needs to finish many more calculations within the time budget of the fast orbit feedback system. At NSLS-II, we proposed a FPGA-based fast orbit feedback algorithm solution for such an approach.

Fig. 11 shows the structure of an NSLS-II orbit feedback system with individual eigenmode compensation.
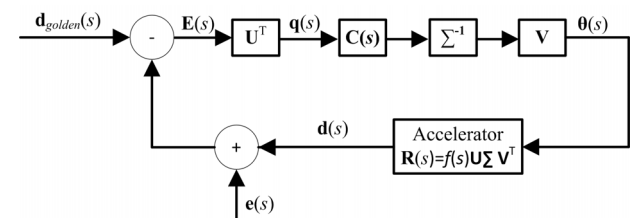

Figure 11: Structure of orbit feedback system with SVD.

In Fig.11, $\mathbf{R}(s)$ is the response matrix of the accelerator. It is simplified to the multiplication of a single transfer function $f(s)$ and a constant matrix $\mathbf{R}_0$ [29]. The $f(s)$ includes the frequency response of the BPM and the corrector. Using the common SVD notations, we assume there are M BPMs and N fast correctors in the orbit feedback system. When $M \geq N$, the SVD of response matrix R(s) can be written as:

$$\mathbf{R}(s) = f(s)\mathbf{R}_0 = f(s)\mathbf{U\Sigma V}^{\mathrm{T}} \qquad (1)$$

where $\mathbf{U}$ is an MxN matrix with an orthonormal column vector set. $\mathbf{V}^{\mathrm{T}}$ is the transpose of the NxN matrix $\mathbf{V}$, which also has an orthonormal column vector set. Σ is an NxN diagonal matrix with non-negative elements, and its eigenvectors are referred as the orbit eigenmodes. The N-dimension space constructed by these eigenmodes is referred as eigenspace.

In Fig. 11, $\boldsymbol{\theta}(s)$ is the corrector strength and $\mathbf{d}(s)$ is the BPM measurement. $\mathbf{e}(s)$ represents the system noises, which include the contributions from quads center motion, BPM motion, BPM electronics noises, and angular kicks from stray field errors. $\mathbf{d}_{golden}(s)$ is the reference orbit, and $\mathbf{E}(s)$ is the orbit error.

From Fig. 11,

$$\mathbf{q}(s) = \mathrm{U}^{\mathrm{T}}\mathbf{E}(s) \qquad (2)$$

$\mathbf{q}(s)$ is the orbit error's representation in eigenspace. It can be shown that in eigenspace, each eigenmode is independent and can be treated as a SISO problem [29].

In eigenspace, we need to design compensation for each eigenmode, or,

$$\mathbf{C}(s) = \begin{bmatrix} c_1(s) & 0 & 0 & 0 \\ 0 & c_2(s) & 0 & 0 \\ . & . & . & . \\ 0 & 0 & 0 & c_N(s) \end{bmatrix} \quad (3)$$

The goal is to design the SISO compensation $c_i(s)$ to suppress the noises for the ith eigenmode. The MxN MIMO problem is converted into N SISO problems in eigenspace.

Even though the above discussions are for continuous systems, they are valid for discrete digital systems. Today, most of the fast orbit feedback subsystem (BPM data, calculations, power supplies, etc.) are discrete systems. As is well-known in control theory [30], the Laplace transform mentioned above should be replaced by a Z-transform; the goal is to design N digital compensations in eigenspace, and Eq.(3) becomes:

$$\mathbf{C}(z) = \begin{bmatrix} c_1(z) & 0 & 0 & 0 \\ 0 & c_2(z) & 0 & 0 \\ . & . & . & . \\ 0 & 0 & 0 & c_N(z) \end{bmatrix} \quad (4)$$

Here the $c_i(z)$ refers to the Z transform of the digital compensator for the ith eigenmode.

Implementation

The NSLS-II fast orbit feedback system is designed to suppress noises up to a few hundred Hertz. To achieve this goal, the orbit feedback sampling/correction frequency needs to be in the KHz range. NSLS-II's orbit feedback system's sampling/correction frequency is 10 KHz. During one sampling/correction cycle, the system needs to finish BPM data transfer, orbit feedback calculations, and power supply setpoints delivery. For a large distributed system, the system architecture needs to be carefully designed to meet the stringent time budget.

At NSLS-II, each BPM is capable of generating beam position data in 10 KHz for orbit feedback calculation. It is a challenge to quickly deliver all BPM data around the ring for the global orbit feedback calculation. Due to the large number of BPMs, serial link architecture is more suitable than a tree or star architecture. Fig. 12 shows the NSLS-II orbit feedback architecture. Fig. 12(a) shows the architecture of the orbit feedback system in one cell. Fig. 12 (b) shows the 30 cells around the storage ring. In each cell, a BNL-developed multi-Gbit/second serial device interface (SDI) is used to transfer data from the 6 BPMs to the cell controller. The similar SDI link delivers each cell's BPM data around the ring. It takes less than 14 μs to deliver the 180 BPMs' data (X and Y positions) to each

of the cell controllers where the orbit calculation is carried out. The cell controller also has 100Mbit/second serial links to the power supply controllers (PSCs) to send the corrector set points. The communications are controlled by the FPGA chips in the cell controller, BPM, and power supply controller.
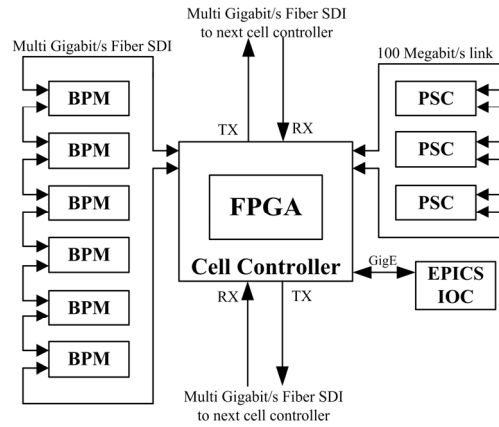
(a) Structure in one cell.
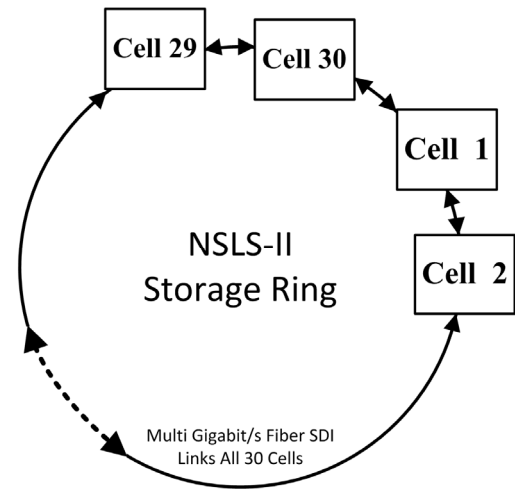
(b) 30 cells in storage ring.

Figure 12: NSLS-II orbit feedback system.

For the NSLS-II fast orbit feedback system, the compensation in each eigenmode allows us to study and design the system in the frequency domain using standard SISO control theory. On the other hand, this approach requires a large number of calculations [10,31-33]. To calculate one corrector setpoint requires an order of NxM multiplications and accumulations [10,33], where M is the BPM number and N is the corrector number. For a global orbit feedback system, M and N are on the order of hundreds. Moreover, the calculation needs to be done within one feedback cycle (100μs for 10KHz feedback). A fast computation system is needed to overcome this computation challenge. At NSLS-II, a powerful FPGA chip-in-cell controller is used for the global orbit feedback calculation, not only because FPGA has many DSP blocks for high-speed calculation, but also because it

can carry out the calculation in parallel. The individual eigenmode compensation algorithm can take advantage of the parallel DSP features and thus greatly reduce the amount of calculation time.

Figure 13 shows the FPGA implementation of the NSLS-II global orbit feedback calculation in each cell controller. There are 180 BPMs and 90 fast correctors in the system. The eigenspace decomposition and the eigenmode compensation ($c_i(z)$) are carried out in parallel for all the eigenmodes. The corrector setpoint calculations are also done in parallel. The total calculation time is less than 10 μs.
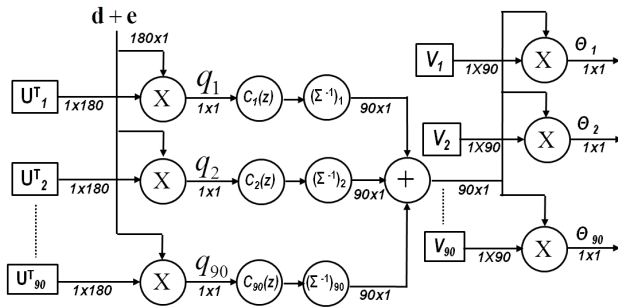

Figure 13: NSLS-II orbit feedback calculation.

SUMMARY

The NSLS-II BPM systems have been optimized, procured, and installed. The injector BPMs have been fully integrated and tested with high-level control operational software. The linac and linac-to-booster transfer line BPMs were commissioned with beam in the Spring of 2012; the remaining injector BPM system commissioning is scheduled for Fall 2013. The storage ring BPM installation is complete and system integration testing is in progress, with test completion expected by November, 2013. The built-in pilot tone signals in the NSLS-II BPM system are being used to test most of the functionality in the BPM system to the extent possible before beam commissioning starts.

The NSLS-II fast orbit feedback algorithm with eigenmode compensation is discussed. It shows that this algorithm provides better controllability for the orbit feedback system by decoupling the feedback signal into eigenspace and compensating for each eigenmode. It discusses the calculation challenges for this approach. It also shows how the NSLS-II FOFB architecture is able to solve this challenge.

REFERENCES

[1] NSLS-II Preliminary Design Report, http://www.bnl.gov/nsls2/project/PDR

[2] F. J. Willeke, "Status of NSLS-II project," PAC11.

[3] T. Shaftan, "Status of NSLS-II Injector," IPAC13.

[4] R. Fliller, "Results of NSLS-II Linac Commissioning," IPAC13.

[5] S. Krinsky, "Accelerator physics challenges for the NSLS-II Project," PAC09.

[6] S. Sharma, "Optimization of magnet stability and alignment for NSLS-II," PAC11.

[7] V. Ravindranath, "Vibration stability of NSLS-II girder magnet assembly," Medsi08.

[8] B. Kosciuk, "Optimizing the thermal management of nsls-2 RF BPM electronics," BIW12.

[9] L. H. Yu, "The performance of a fast closed orbit feedback system with combined fast and slow correctors," EPAC08.

[10] Y. Tian, "NSLS-2 fast orbit feedback with individual Eigenmode compensation," PAC11.

[11] Kiman Ha, "NSLS2 beam position monitor embedded processor and control system," ICALEPCS11.

[12] P. Cameron, "BPM button optimization to minimize distortion due to trapped mode heating," PAC09.

[13] I. Pinayev and A. Blednykh, "Evaluation of heat dissipation in the BPM buttons," PAC09.

[14] I. Pinayev and O. Singh, "Evaluation of BPM geometry to optimize sensitivities for NSLS-II," NSLS-II internal technical note, 2009.

[15] A. Blednykh, "Wake Loss Simulations at NSLS-II", Diamond Light Source Workshop, 2013.

[16] I. Pinayev, "Optimization of Small-Aperture Beam Position Monitors for NSLS-II Project," BIW10.

[17] W. Cheng, B. Bacha & O. Singh, "NSLS2 Beam Position Monitor Calibration," BIW12.

[18] A. Blednykh, "NSLS-II BPM system protection from rogue mode coupling," PAC2011.

[19] B. Kosciuk, "Development and testing of carbon fiber composite chamber supports for nsls2," PAC11.

[20] B. Kosciuk, *et al.*, "Development of high stability supports for nsls2 BPMs," PAC09.

[21] W. Cheng, "Vibration Measurement and its effect on beam stability at nsls2," IBIC13, this conference.

[22] K. Vetter, "NSLS-II RF beam position monitor," PAC11.

[23] K. Vetter, "NSLS-II RF beam position monitor update," BIW12.

[24] W. Cheng, "Performance of NSLS-II button BPM," IBIC13 – this conference.

[25] G. Danby, "Design and measurement of the NSLS-II corrector" PAC09.

[26] G. Ganetis, "Fast orbit corrector workshop," NSLS-II 2009.

[27] N. Hubert, "Global orbit feedback systems down to DC using fast and slow correctors," DIPAC09.

[28] O. Singh *et al.*, PAC 91, p. 1528.

[29] Y.Tian, L.H.Yu, "Handbook of Accelerator Physics and Engineering," edited by A Chao , etc . 2nd edition , p . 624 (2013).

[30] A. Oppenheim, *et al.*, "Signals and Systems" (1996).

[31] A. Terebilo et al., EPAC06, p. 3035.

[32] D.Teytelman, PAC03, p. 318.

[33] M.G. Abbott et al., EPAC08, p. 32.